


Article

Tuning the Photocatalytic Performance of Ni-Zn Ferrite Catalyst Using Nd Doping for Solar Light-Driven Catalytic Degradation of Methylene Blue

Pooja Dhiman¹, Garima Rana¹, Elmuez A. Dawi² , Amit Kumar¹, Gaurav Sharma^{1,*} , Arun Kumar³ and Jayati Sharma¹

¹ International Research Centre of Nanotechnology for Himalayan Sustainability (IRCNSHS), Shoolini University, Solan 173229, India

² Nonlinear Dynamics Research Centre (NDRC), College of Humanities and Science, Ajman University, Ajman P.O. Box 346, United Arab Emirates

³ Department of Physics, Kurukshetra University, Kurukshetra 136119, India

* Correspondence: gaurav8777@gmail.com

Abstract: In this paper, we describe the creation of a moderate band gap Nd-substituted Ni-Zn ferrite as a nano photo catalyst via a simple and cost-effective process of solution combustion. Nd substitution alters the crystallite size, shape, band gap, and magnetic characteristics of Ni-Zn ferrite significantly. Investigations using X-ray diffraction revealed that all samples display a pure phase. The average crystallite size was determined to be between 31.34 and 38.67 nm. On Nd doping, morphology investigations indicated that the shape of nanoparticles changed from approximately spherical to stacked grains. Band gap experiments confirmed the red shift in optical band gap on Nd doping. The synthesized catalysts $\text{Ni}_{0.5}\text{Zn}_{0.5}\text{Fe}_2\text{O}_4$ (Nd0), $\text{Ni}_{0.5}\text{Zn}_{0.45}\text{Nd}_{0.05}\text{Fe}_2\text{O}_4$ (Nd1), and $\text{Ni}_{0.5}\text{Zn}_{0.5}\text{Nd}_{0.05}\text{Fe}_{1.95}\text{O}_4$ (Nd2) have been effectively used for the degradation of methylene blue dye under the solar light irradiation. The sample with Nd substitution on Fe sites had the highest methylene blue degradation efficiency. Nd2 photo catalyst degrades the methylene blue dye with a degradation efficiency of 98% in 90 min of solar light irradiation. The photocatalytic activity is triggered by the existence of oxygen vacancies and a mixed valence state of Ni, Fe, and Nd, as confirmed by the XPS investigation. In addition, the investigations on scavenging reveal that the hydroxyl radical is a reactive component in the degradation process. The degradation route has been investigated in relation to the many potential reactions and discovered reactive substances.

Keywords: ferrite; photo catalysis; magnetic properties



Citation: Dhiman, P.; Rana, G.; Dawi, E.A.; Kumar, A.; Sharma, G.; Kumar, A.; Sharma, J. Tuning the Photocatalytic Performance of Ni-Zn Ferrite Catalyst Using Nd Doping for Solar Light-Driven Catalytic Degradation of Methylene Blue. *Water* **2023**, *15*, 187. <https://doi.org/10.3390/w15010187>

Academic Editor: Zhiliang Zhu

Received: 15 November 2022

Revised: 19 December 2022

Accepted: 27 December 2022

Published: 2 January 2023



Copyright: © 2023 by the authors. Licensee MDPI, Basel, Switzerland. This article is an open access article distributed under the terms and conditions of the Creative Commons Attribution (CC BY) license (<https://creativecommons.org/licenses/by/4.0/>).

1. Introduction

The tremendous use of synthetic organic compounds for a wide range of industrial processes has often led to major contamination of the environment around the world [1]. Color has been identified as the most important contaminant among the numerous contaminants found in wastewaters. In several sectors, dyes are used to color the items they are attached to. As a result, a large amount of colored wastewater is produced. Many types of species are poisoned or endangered by them. Even at low concentrations, the presence of these colors in water is extremely problematic, and the requirement for their removal has been verified [2,3]. One of the most common types of aromatic dyes is called methylene blue (MB). It is used in the textile industry to dye the fabrics [4,5]. These dye components, which are persistent, poisonous, and non-degradable, have the potential to significantly degrade water quality even at small trace levels [6]. Its intrinsic cytotoxic activity and necrotic effects pose a threat to human health in the event of exposure [7]. Various strategies for decolorization have been explored which include adsorption [8,9], chemical oxidation [10], photocatalytic degradation [11–13], and membrane filtration [14].

Ongoing research is aimed at developing photocatalytic materials that can help remediate wastewater contaminated with these dangerous pollutants. Due to the rising hazard of water contamination, the development of advanced cleanup approaches remains a global priority [15]. In this context, photocatalysis has received much interest because it allows organic pollutants to be totally decomposed into harmless end products in an environmentally beneficial way [16–19]. Furthermore, this approach can prevent the production of secondary hazardous byproducts. Better catalysts are possible because of recent advances in nanoscience. The large surface area supplied by nanoparticles leads to higher catalytic activity. Photocatalysis is a high-efficiency, low-cost advanced oxidation technique based on the production of highly reactive and oxidizing hydroxyl radicals [18,20]. The photocatalytic efficacy of every photocatalyst is directly influenced by its capacity to absorb light. Solar energy contains around 50% visible light and only 4% UV light; photocatalytic degradation using this spectrum is preferable to UV light [21]. As a result, using semiconducting systems with enhanced absorption in the visible area is favorable and can result in better photocatalytic activity. Still, different ideas have been put forward to deal with problems such as achieving high efficiency, making it easily recoverable, and making sunlight-driven catalysis possible. Recently, many scientists have been interested in magnetic ferrites-based photocatalysts because they have a good band gap (2–3 eV) and a wide range of absorption [22]. Ferrites are known for their diverse applications such as high frequency applications [23], catalysis [24,25], sensors [26], biomedical applications [27], anti-corrosion activities [28], and much more [29]. The nickel ferrite has been intensively explored because of its inexpensive cost, narrow band gap of 2.2 eV, eco-friendly behavior, higher resistivity, and magnetic behavior [30]. Magnetic nickel-zinc ferrite has attracted much attention because of its peculiar magnetic properties, and catalytic applications as well as its excellent stability, ease of processing, and repeatability [31,32]. Because of its unusual features, Ni–Zn ferrite, a novel nanomaterial, has recently become the focus of many studies aimed at better understanding its manufacture and utilization. By substituting other metals, the photocatalytic performance of nickel ferrite-based photocatalysts can also be enhanced further. The rare-earth-substituted nickel-zinc ferrite could be used as a photocatalyst because it can absorb a large amount of visible light, is very durable, and can be reused and recycled. Rare-earth ions are prospective replacements for enhancing the characteristics of spinel ferrites. The rare-earth elements have unpaired 4f electrons and a significant spin–orbit coupling of angular momentum. The 4f shell of rare-earth elements is protected by 5s² 5p⁶ and is little influenced by the surrounding ion field. The addition of rare-earth ions to spinel ferrites and the presence of 4f–3d couplings in ferrites can enhance the magnetic and affect the charge transport capabilities of NiFe₂O₄ ferrites [33]. Ni–Zn ferrites can be synthesized using a variety of processes, including the oxalate precursor approach [34] co-precipitation [35], ceramic approach [36], hydrothermal treatment [37], and combustion approach [38]. Among others, combustion procedures are preferred because of their simplicity, adaptability, speedy completion of the reaction, and homogeneous addition of dopant [39]. The use of fuel materials such as hydrazides, urea, glycine, and citric acid during this process helps in the homogeneous mixing of the solution. The magnetically recoverable photocatalysts are highly desirable as they help in the easy and complete separation of the catalyst from the rest of the medium [40]. When compared to typical photocatalysts, ferrites have the potential to significantly improve catalyst recovery and reusability without resorting to centrifugation or flotation [41]. Aside from that, the most promising way to produce highly efficient photocatalysts is to use nanoferrites with a high surface area to volume ratio and quantum confinement. Hammouche et al. fabricated zinc-doped nickel ferrite nanoparticles by a facile auto-combustion method using glycine as fuel and studied the behavior of nanoparticles for the photocatalytic degradation of methylene blue dye. The degradation rate of methylene blue solution increased successively with Ni doping and photocatalytic activity up to 98%, which can perform as an environmentally friendly, easily isolable, and recyclable photocatalyst for water treatments [42]. Harish et al. prepared Nd-doped nickel ferrite nanoparticles and

study their catalytic applications. To make NiFe_2O_4 photo catalytic, the neodymium substitution into nickel ferrite results in an enormous transformation of the previously inactive NiFe_2O_4 [43]. This may be owing to the Nd^{3+} substitution, which reduces the nickel ferrite band gap. The choice of Nd as dopant can be verified from literature where Nd doping into ferrites has resulted into varied visible light absorption, red shift of the band gap, altered charge transport properties, and enhanced saturation magnetization, which can directly or indirectly favor the photocatalytic performance of the catalysts [44,45]. Motivated by incredible potential of Ni nano ferrites as photo catalyst, we explored the ability of Nd doped Ni-Zn nano ferrite system for the photo catalysis of methylene blue dye.

2. Materials and Methods

2.1. Materials

To synthesize Nd substituted Ni-Zn ferrite nanoparticles, nickel nitrate ($\text{Ni}(\text{NO}_3)_2 \cdot 6\text{H}_2\text{O}$, $\geq 97\%$; Sigma-Aldrich, St. Louis, MO, USA), iron nitrate ($\text{Fe}(\text{NO}_3)_3 \cdot 9\text{H}_2\text{O}$, $\geq 99.95\%$; Sigma-Aldrich), $\text{Nd}(\text{NO}_3)_3 \cdot 6\text{H}_2\text{O}$, and glycine ($\text{C}_2\text{H}_5\text{NO}_2$, $\geq 99.7\%$; Merck, Rahway, NJ, USA) were used as raw materials.

2.2. Preparation of Catalysts

The solution combustion approach is used to fabricate nano crystalline neodymium-substituted nickel-zinc ferrite nanoparticles. The raw materials employed include iron nitrate, nickel nitrate, neodymium nitrate, zinc nitrate, and glycine in the desired ratios. Nitrates (oxidizers) and glycine (fuel) were kept at a 1:1 molar ratio and were diluted in double distilled water with the aid of magnetic stirrer. The resultant solution was heated to 80°C with continual stirring. The solution was subjected for combustion in the open air at 120°C after complete dissolution, resulting in a fine fluffy powder. Calcination acquired powders at 750°C for 4 h in a muffle furnace yielded the final product. The resulting fine powder is further utilized for characterizations purpose. The synthesized samples $\text{Ni}_{0.5}\text{Zn}_{0.5}\text{Fe}_2\text{O}_4$, $\text{Ni}_{0.5}\text{Zn}_{0.45}\text{Nd}_{0.5}\text{Fe}_2\text{O}_4$, and $\text{Ni}_{0.5}\text{Zn}_{0.5}\text{Nd}_{0.5}\text{Fe}_{1.95}\text{O}_4$ were labeled as Nd0, Nd1, and Nd2, respectively.

2.3. Characterization Details

X-ray diffraction (XRD; PHILIPS) tests with $\text{Cu-}\alpha\text{K}$ radiations in the region of $20\text{--}80$ degree 2θ variations were used to describe the produced samples to collect the crystal structure information and various structure related parameters. The XRD pattern was further fitted with the help of Rietveld fitting using Fullprof software. Transmission electron microscopy was used to examine the nanoparticles' shapes and sizes (TEM, JEOL JEM 2100, Peabody, MA, USA). The surfaces of catalysts were analyzed using scanning electron microscopy (Nova Nano SEM-450, Peabody, MA, USA). The magnetic characteristics of manufactured nanoparticles have been investigated using a vibrating sample magnetometer (Lakeshore 7410, Columbus, UH, USA). The valence state and the elemental confirmation was done with the help of X-ray photoelectron spectrometer (Semmer, UK). The resulted core level spectra were fitted with XPS peakfit41 software. The optical band gaps were determined using Tauc's plot and a double beam spectrophotometer to better understand the material's optical characteristics. The electrochemical impedance spectroscopy was utilized to check the charge transfer capacity of the catalysts. The experiment was performed at CHI660E electrochemical workstation by using three electrodes. The working electrode consists of ferrite modified GCE electrode, Ag/AgCl as reference electrode and Pt as counter electrode. 0.3 M sodium sulphate solutions were used as electrolyte.

2.4. Photo Catalytic Degradation of Methylene Blue

Photocatalytic experiments in natural sunlight are used to evaluate the photocatalytic performances of the synthesized catalysts. The experiment place was Solan, India—i.e., 30.9045°N , 77.0966°E , Shivalik Hills, Himalayan region, and performed in an open atmosphere. The average intensity as measured by luxmeter was $29 \pm 5 \times 10^3$ lx. The

experiments were performed in a physical arrangement: Pyrex vessel having double-wall jacket for water circulation to maintain regular temperature, with continuous stirring. Methylene blue (Sigma-Aldrich > 98%) has been considered as target organic pollutant. In the experiment, 25 mg catalyst was dispersed in 100 mL of aqueous methylene blue (20 mg/L). The resulting solution was allowed to place in dark for 60 min for adsorption–desorption equilibrium. Thereafter, the solution was allowed to irradiate under light source. An aliquot from the suspension was taken after regular interval of time and then allowed to centrifuge for the filtration of catalyst. With the help of UV-visible spectrophotometer, degradation of methylene blue was determined. The percentage degradation of pollutant is given by the relation [46]:

$$\% \text{ degradation efficiency} = \frac{C_0 - C_t}{C_0} \times 100 \quad (1)$$

where C_0 and C_t represent the concentration of methylene blue at $t = 0$ and $t = t$ time, respectively. The kinetics of the degradation is determined using the relation given by:

$$\ln \frac{C_0}{C_t} = kt \quad (2)$$

In the above equation k represents the rate, and C_0 , C_t represents the concentration of methylene blue at $t = 0$ and $t = t$ time, respectively.

3. Results and Discussions

3.1. Characterization of the Catalysts

X-ray diffraction has been utilized for the structural information of the catalysts. The X-ray diffraction patterns of all synthesized samples recorded in the range $2\theta = 0\text{--}90^\circ$ are shown in Figure 1. The planes (220), (311), (222), (400), (422), and (511) present in the diffraction patterns confirm that all the samples have the cubic spinel structure [47]. The major peaks are indexed as per JCPDS File 10-0325. The absence of any other peak denies the possibility of any secondary phase formation for all samples. The crystallite size (D) is calculated using the Scherrer formula [48].

$$D = \frac{K\lambda}{\beta \cos \theta} \quad (3)$$

where K is the shape constant, λ is the wavelength of X-ray used for diffraction, β corresponds to full width at half maxima of the diffraction peaks, and θ is the corresponding Bragg's angle. The average crystallite size of Nd0, Nd1, and Nd2 was calculated and the size was in the range 31.34–38.67 nm. The peak (311) was chosen for calculating the lattice constant (a). The lattice constant (a) is calculated using Bragg's equation given by:

$$d = \frac{a}{\sqrt{h^2 + k^2 + l^2}} \quad (4)$$

where d refers to inter planar spacing and h , k , and l are corresponding Miller indices. The calculated values of lattice parameters are 8.3346, 8.3697, and 8.3508 Å for Nd0, Nd1, and Nd2, respectively. The lattice constant value of the doped Ni-Zn ferrite sample is slightly higher than that of unsubstituted Ni-Zn ferrite samples. The reason for this is that the ionic radii of Nd^{3+} ion (1.16 Å) is higher than the Fe^{3+} ion (0.78 Å) and Zn^{2+} ion (0.82 Å). The replacement of larger ionic radii with slightly less ionic radii results in an increase of lattice parameters [49]. Furthermore, TEM analysis was performed for Nd2 sample and presented in Figure 1b. TEM image confirmed that the particles reside in nano dimensions and supported the observed XRD results. Moreover, SAED pattern (Figure 1c) (selected area electron diffraction) shows the bright and regular spots, which reveal the highly crystalline nature of Nd2 sample.

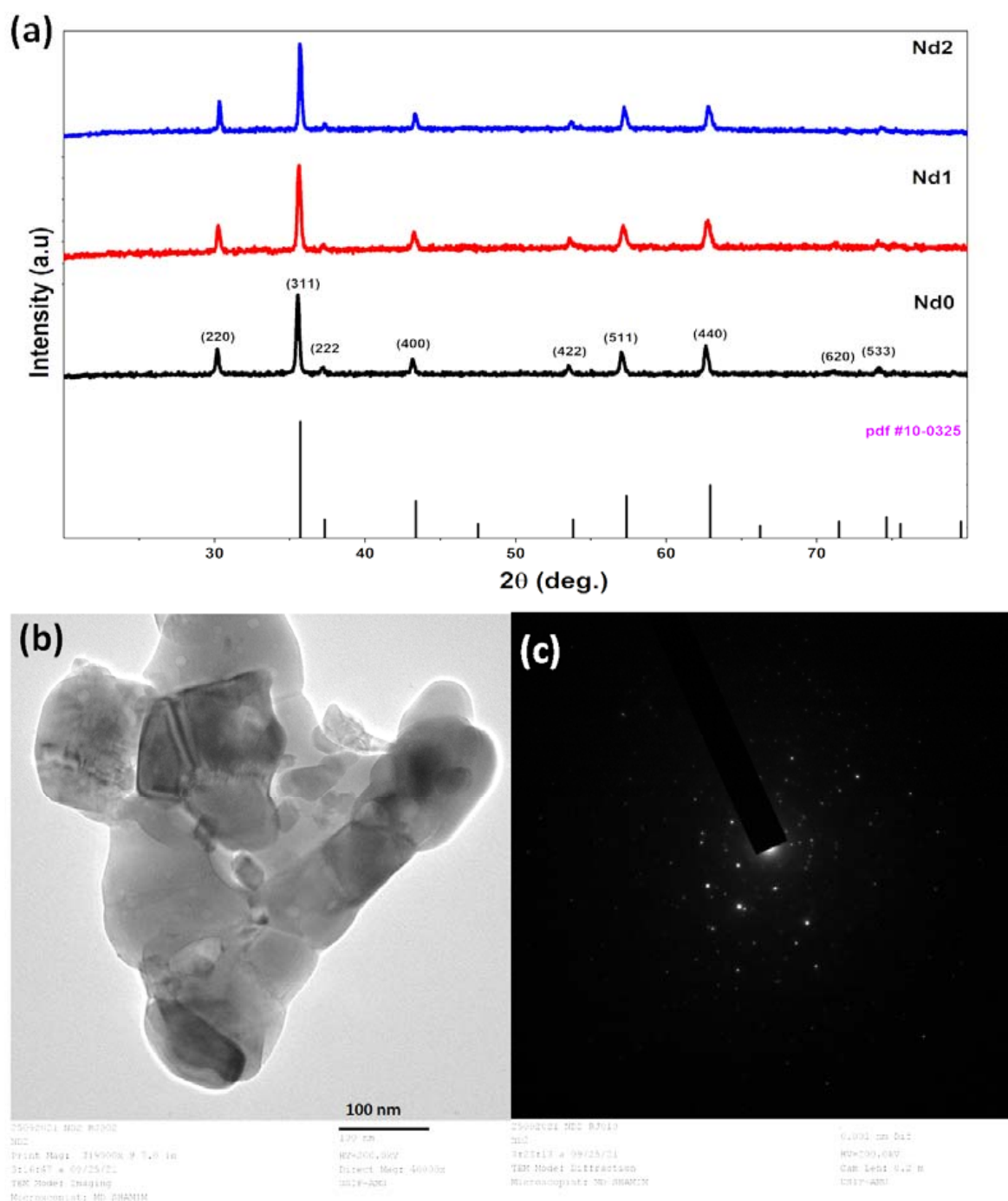


Figure 1. (a) X-ray diffraction pattern for synthesized catalysts, (b) TEM image for Nd2 sample, and (c) corresponding SAED pattern.

On the XRD patterns, Reitveld fitting is conducted to further check the phase purity of the produced catalysts. The XRD patterns are compatible with a cubic phased spinel structure with space group symmetry $Fd\bar{3}m$. The fitted XRD patterns are shown in Figure 2. It is very evident from the pattern that there are no secondary phases present in the samples. All observed peaks are the characteristic peaks of cubic structure. The crystallite volume follows the same trend as observed for lattice parameters. All structural parameters derived from the fitting of the pattern are listed in Table 1.

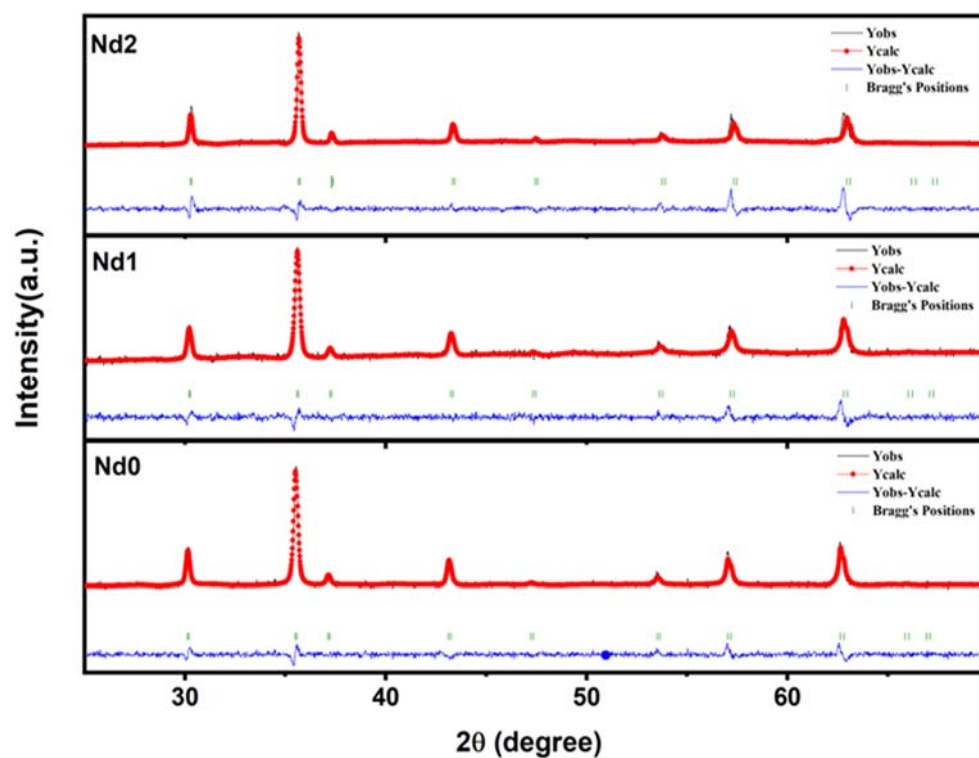


Figure 2. Rietveld refined XRD pattern of Nd0, Nd1, and Nd2 samples.

Table 1. Rietveld refined structural parameters.

Sample	Nd0	Nd1	Nd2
Bragg R-Factor	5.58	11.00	6.00
Rf Factor	4.45	9.36	4.48
Volume	581.107	588.942	584.982
R _p	62.00	83.8	77.7
R _{wp}	28.00	39.8	34.0
R _e	26.00	27.00	31.7
χ^2	1.123	2.181	1.147

3.2. SEM Analysis and Elemental Mapping

The morphology of the surfaces of synthesized catalysts was analyzed by scanning the surfaces of the catalysts using a scanning electron microscope. Figure 3a–c shows the recorded scanning electron micrographs for synthesized nano ferrite samples. Morphology of bare Ni-Zn ferrite sample exhibits the roughly spherical shaped grains. The Nd0 sample exhibits uniform particle size distribution in comparison to other samples. However, Nd1 and Nd2 sample shows quite stacked structure of grains. Nd substitution has resulted in changed morphology in the host Ni-Zn ferrite matrix. Besides morphology, dopant confirmation is done by analyzing elemental mapping. Figure 3d–i presents the elemental images for Nd2 sample. Mapping micrographs reveals the uniform distribution of Ni, Zn, Nd, Fe, and O elements for Nd2 sample.

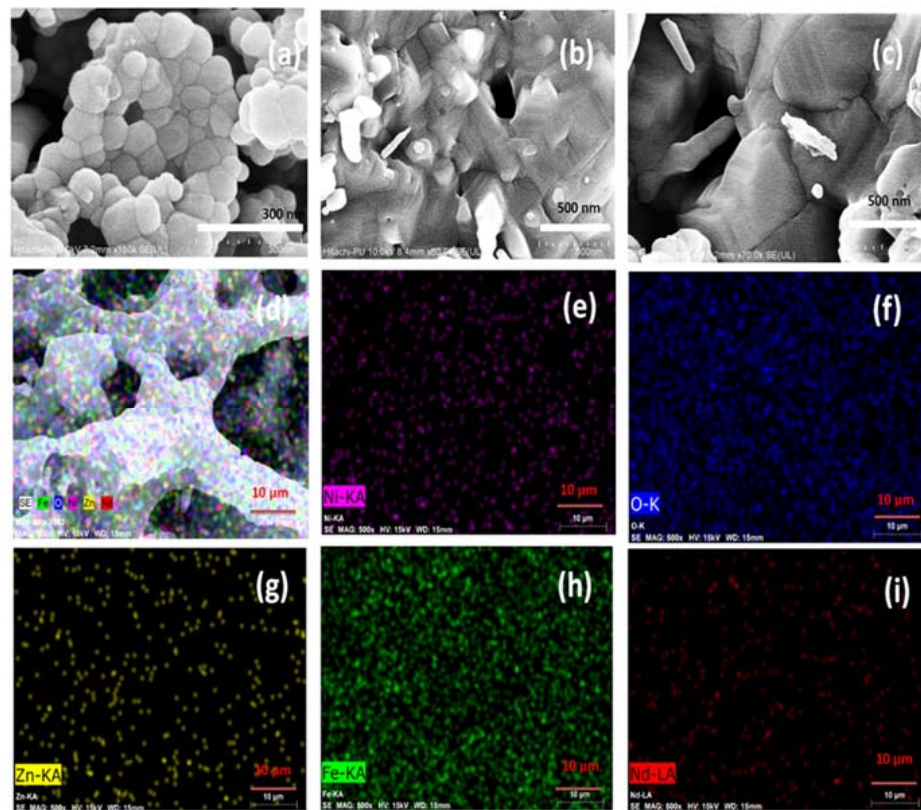


Figure 3. SEM images for (a–c) Nd0, Nd1, and Nd2 samples. (d–i) Elemental mapping for Nd2 sample.

3.3. Band Gap Estimation and Electrochemical Response Studies

The appropriate band gap of the material is a main need to function as efficient photo catalyst. In this view, the band gap of the catalysts is evaluated using UV-visible spectroscopy. Figure 4 shows Tauc plot ($\alpha h\nu^2$ vs. $h\nu$) for the Nd0, Nd1, and Nd2 catalysts. The band gap values for all catalysts are derived by extrapolating the data points from the higher energy area. The Nd0 band gap has been measured to be 2.11 eV. With the substitution of Nd ions with Zn and Fe, the band gap value decreases. The calculated band gap for samples of Nd1 and Nd2 is 1.68 eV and 1.72 eV, respectively. Such observed behavior indicates that quantum confinement has no role in this situation [50]. The reduction in the band gap may be attributed to the fact that Nd doping has resulted in the creation of additional meta-stable energy levels by Nd 4f electrons. The meta-stable states lie close to the conduction band edge [51]. The enhanced apparent absorption and reasonable levels of band gap energy indicate that the samples can be used as photocatalysts. To further check the charge transfer capacity of the catalysts, EIS spectra (Nyquist plots) were collected using catalysts modified electrodes. Figure 4c shows the observed EIS spectra for Nd doped catalysts. It is evident from the spectra that Nd2 has lowest impedance. Nd2 modified electrode showed the lowest radius of the semicircle obtained in EIS spectra, indicating the highest charge transfer capacity of the catalysts, while others have slightly more radius of the semicircle conveying less charge transfer capacity of the catalysts. The observed results indicate that Nd doping at Fe sites results in an increase of charge transfer capacity of Ni-Zn ferrites. The doping has reduced the charge recombination rate of carriers and promoted the carrier flow rate, which are prime requirement for photo catalysis.

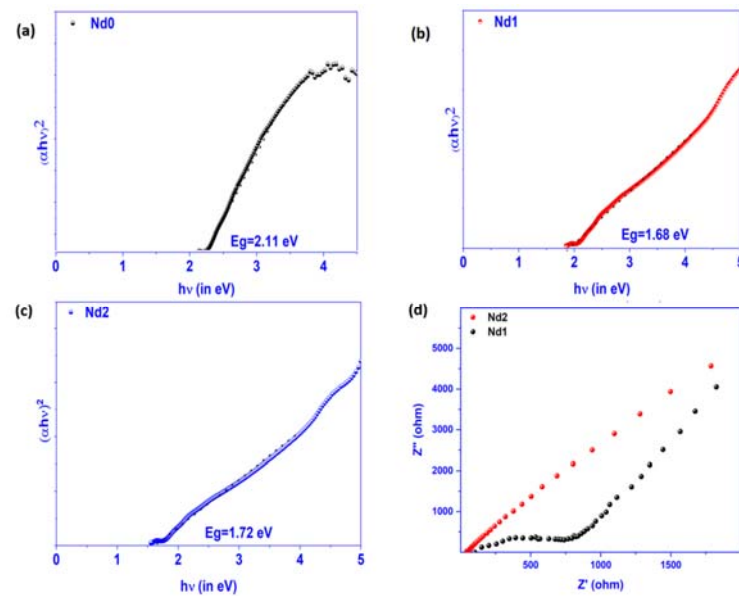


Figure 4. (a–c) Tauc's plot for Nd0, Nd1, and Nd2 samples, (d) EIS spectra for Nd1 and Nd2 catalysts.

3.4. X-ray Photo Electron Spectroscopy Studies

The valence state information shows a surprising significance in influencing the charge transport behavior of the photo catalysts, thus likewise altering their degradation efficiencies. In this view, all the samples have been characterized with X-ray photoelectron spectroscopy for further investigation. Figure 5a presents the de-convoluted Fe 2p spectra for all synthesized samples. Fe 2p spectra for all samples mainly possessed two main peaks assigned to Fe 2p_{3/2} and Fe 2p_{1/2} which arises due to spin orbit coupling along with their shoulder peaks. The major peaks are further sub-divided into other peaks. For Nd0 sample, the lower binding energy Fe 2p_{3/2} peaks are located at 710.45 and 712.33 eV, respectively. The observed peaks' position matches well with the reported values showing two different environments of Fe states, i.e., octahedral as well as tetrahedral. The observed peak at 724.39 eV is assigned to Fe 2p_{1/2} state. These peak positions are in close agreement with the previously reported values for Fe³⁺ states [52]. The other observed peaks at 717.46 and 731.60 eV are referred to as shoulder peaks associated with spin coupling splitter states. However, the positions of all major peaks corresponding to 3/2 and 1/2 states take a slight leftward shift for Nd1 and Nd2 samples. The results indicate that Nd substitution may promote the creation of the Fe²⁺ state along with the Fe³⁺ state in the samples. The exact contributions of Nd substitution on Ni environment have been further analyzed by de-convoluting Ni 2p spectra, as shown in Figure 5b. The observed peaks at 854.80 and 872.34 eV correspond to the Ni 2p_{3/2} and Ni 2p_{1/2} states confirming the Ni³⁺ state of the Nd0 sample. Peaks residing at 856.57 and 873.97 eV signify the presence of Ni²⁺ state. Other peaks are satellite peaks associated with 3/2 and 1/2 states of Ni 2p. Ni is confirmed to have mixed valence state for Nd0 catalyst, which can serve as source for carriers in redox reactions during catalysis. A minor shifting of peak positions takes place in Nd substituted samples. Such a pattern is expected as Nd has made changes in the Ni-Zn ferrite matrix. The presence of any oxygen-related defects inside the catalyst is also investigated using de-convoluted oxygen 1s spectra (Figure 5c). The Nd0, O1s spectra are a combination of two peaks at 529.68 and 531.22 eV. The low binding energy peak is the characteristic peak of the metal-oxygen bond, and the higher binding energy peak corresponds to the loosely bound oxygen or adsorbed oxygen on the surface of the catalyst [53]. Similar behavior is observed for Nd1 sample with slight shift of characteristic peak on higher binding energy side. The spectra obtained for Nd2 are, however, slightly different and fitted with an additional peak. In addition to the low and higher energy peaks, the mid-energy peak is situated at 530.14 eV. This peak is attributed to the presence of oxygen vacancies in the

catalyst. The results indicate that the Nd2 catalyst contains oxygen vacancies and has adsorbed oxygen on its surface. The Zn 2p spectra are also examined for any changes in the Zn environment caused by Nd substitution. Zn 2p spectra are fitted with two major and two minor peaks, indicating two different environments of Zn ions in all samples, which might be due to the tetrahedral and octahedral environment in the cubic structure of ferrites (Figure 5d). It is necessary to probe the valence state and environment of Nd ions also. Nd 3d fitted XPS spectra are shown in Figure 6. Nd 3d_{5/2} spectra are fitted with three peaks for both Nd1 and Nd2 samples. In general, Nd³⁺ peak occurs at 982.50 eV, while Nd²⁺ resides at 980.30 eV [54]. The peaks observed at 982.64 and 882.67 eV confirm the presence of Nd³⁺ in both the samples. In case of Nd substituted Zn ferrite nanoparticles, Nd 3d_{5/2} and Nd 3d_{3/2} have been reported to occur at 981.1 and 1003.2 eV, respectively [55]. The peak observed at 980.10 eV indicates the presence of the Ni²⁺ state in the Nd2 sample. According to the literature, the characteristic peak of metallic Nd (Nd clusters) occurs at 980.9 eV, implying that there is no metallic Nd or Nd-Nd environment in either sample. Such results deny the presence of any secondary phases in either of the samples. All observed binding energies are listed in Table 2. In short, XPS analysis confirms the presence of mixed valence states of Ni and Fe in both Nd doped catalysts and mixed valence states of Nd in the Nd2 catalyst. The presence of mixed valence states may coordinate the charge transfer of carriers and play a significant role in redox reactions.

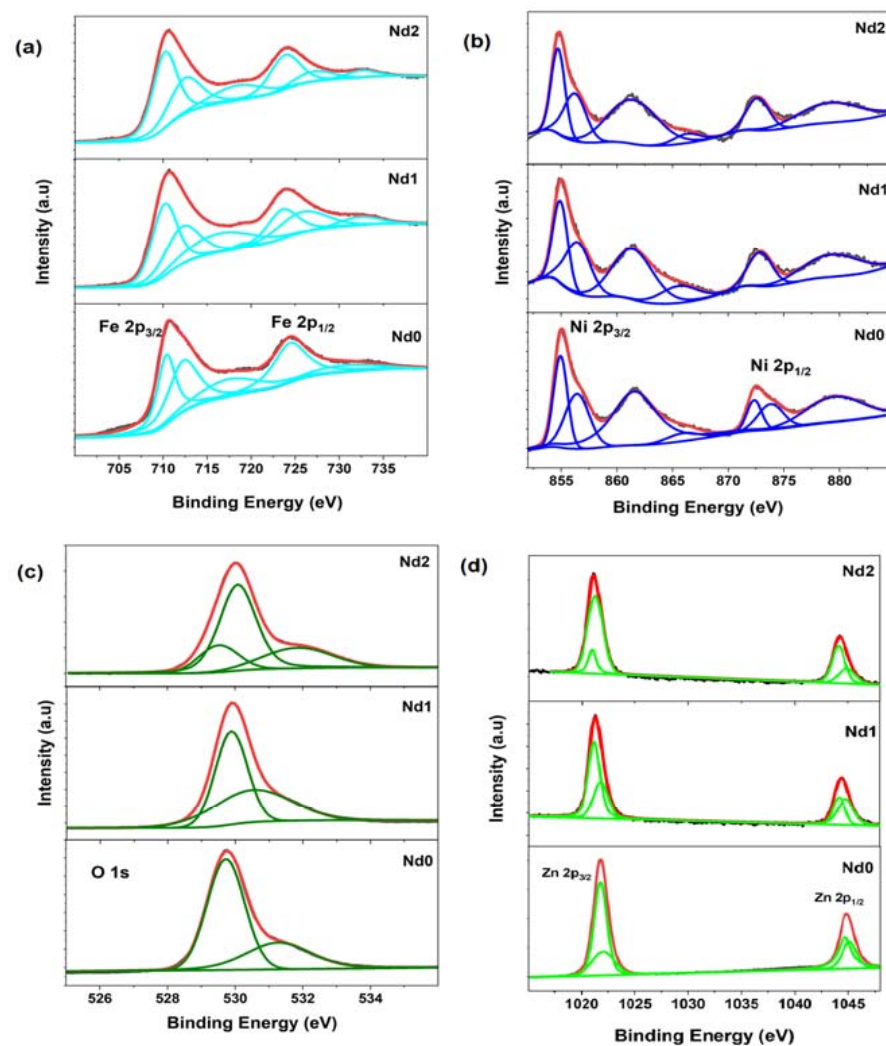


Figure 5. De-convoluted core level spectra for (a) Fe2p, (b) Ni 2p, (c) O1s, and (d) Zn 2p state.

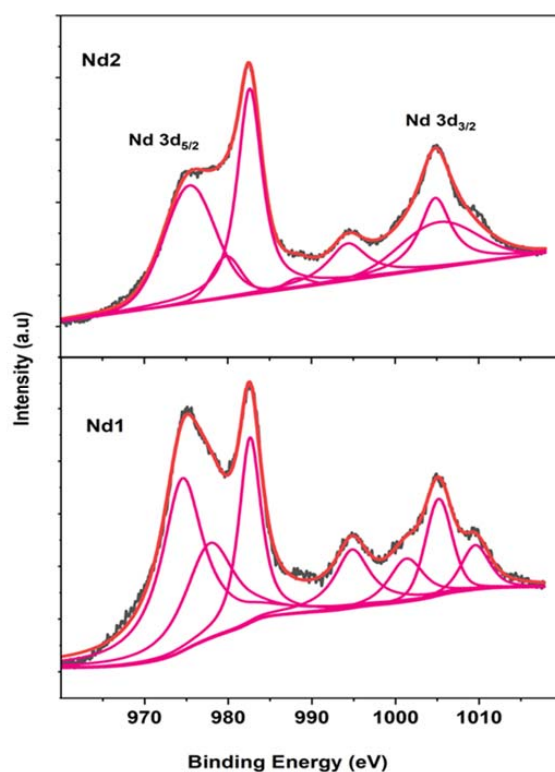


Figure 6. Core level de-convoluted spectra for Nd 3d state.

Table 2. Binding energy of all constituent elements of synthesized catalyst using de-convoluted XPS spectra.

De-Convolved Peak Positions of Fe 2p Spectra (in eV)					
Nd0	710.45	712.33	717.46	724.39	731.6
Nd1	710.30	712.31	716.72	723.75	726.17, 732.18
Nd2	710.35	712.88	718.49	724.01	727.21, 732.7
De-convoluted peak positions of Ni 2p spectra (in eV)					
Nd0	854.80, 856.57	861.46	866.20	872.34, 873.97	879.67
Nd1	854.87, 856.4	861.16	865.75	872.86	879.46
Nd2	854.58, 856.35	861.24	866.65	872.65	879.09
De-convoluted peak positions of O 1s spectra (in eV)					
Nd0	529.68	-	-	-	531.22
Nd1	529.87	-	-	-	530.60
Nd2	529.46	-	530.14	-	531.85
De-convoluted peak positions of Zn 2p spectra (in eV)					
Nd0	1121.70	1122.10	1044.62	-	1045.36
Nd1	1021.31	1021.95	1044.10	-	1044.92
Nd2	1020.78	1021.35	1044.37	-	1045.31
De-Convolved Peak Positions of Nd 3d Spectra (in eV)					
Nd1	974.48, 978.34	982.67	994.58	1001.82, 1005.35, 1009.70	-
Nd2	976.04, 980.10	982.64	995.02	1001.46, 1005.16, 1009.34	-

3.5. Magnetic Study of the Catalyst

A photocatalyst's strong magnetic behavior is one of its most desirable characteristics. The photocatalyst's magnetic property facilitates recovery and makes it usable after the degradation process over the cycles. Ferrites' magnetic nature makes them suitable to act as magnetically separable photo catalysts and dominate other catalysts that are hard to recover. The magnetic properties of the catalysts are analyzed by recording hysteresis loops (M-H) for the catalyst powder. The experiment is performed at room temperature under the application of 15,000 Oe magnetic field strength. Figure 7 show presents the room temperature magnetization versus field curve for synthesized catalysts. All samples exhibit well saturated hysteresis loops. The saturation magnetization (M_s) values obtained are 71.30, 67.18, and 65.32 emu/g for Nd0, Nd1, and Nd2, respectively. The coercive field (H_c) values are 74.15, 83.19, and 72.17 Oe, respectively. However, the retentivity (M_r) value shows an increasing trend and the observed values are 10.12, 11.26, and 12.52 emu/g for Nd0, Nd1, and Nd2 respectively. The decrease in the saturation magnetization with Nd doping was recently observed by Qian et al. [56]. The magnetic properties of the nanomaterials depend on a number of factors, such as the distribution of cations at respective sites, crystallite size, strain developed in the crystal, and also the anisotropic properties of materials [57]. Even the properties may vary for nanoparticles synthesized using different synthesis routes. The magnetic properties of the ferrites are attributed to the super-exchange interactions resulting from the interactions among the metal ions and mediating oxygen ions [58]. The interaction will lead to the alignment of the spins of ions in antiparallel or parallel way on A (tetrahedral) or B (octahedral) sites and AA or BB sites, respectively. The resulting net difference between the magnetic moments is given by:

$$M_{net} = M_B - M_A \quad (5)$$

where M_B is magnetic moment of the ions at B sites and M_A is the magnetic moment generated at A site. In the Ni-Zn ferrite system, Ni^{2+} ions and Fe^{3+} ions have preference to occupy both tetrahedral as well as octahedral sites, while Zn^{2+} ions have a preference to occupy only tetrahedral sites. Nd^{3+} ions with the magnetic moment of $3.5 \mu_B$ are substituted for Zn^{2+} ($0 \mu_B$) and Fe^{3+} ($5.9 \mu_B$). Ni^{2+} with $2.3 \mu_B$ is residing at both the sites. With the substitution of Nd ions with Fe ions at octahedral sites, the magnetic moment lowers as Nd ions have less magnetic moment value than Fe^{3+} ions, which results in a decrease of resultant magnetic moment value. Nd ions do have a preference for the B site; therefore, when substituted for Zn^{2+} ions, there is possibility that some Fe^{3+} have been shifted from the B site to the A site to accommodate the Nd ions. Therefore, in view of site preference and ionic radii of metal ions, the overall magnetic moment value decreases with Nd ion substitution. However, all prepared samples have sound magnetic properties and can work as magnetically recoverable catalysts.

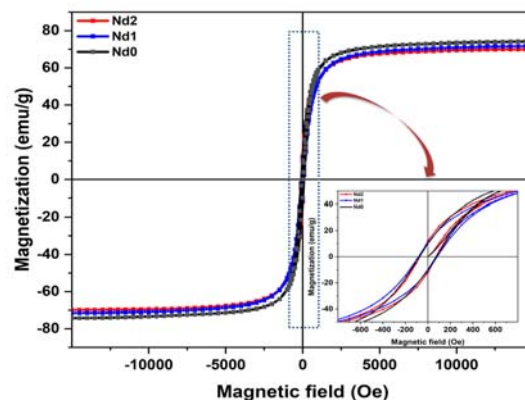


Figure 7. Magnetization versus applied field curves for Nd0, Nd1, and Nd2 samples.

4. Photo Catalytic Activity against Methylene Blue Dye

4.1. Effect of Nd Doping on Ni-Zn Ferrite Catalyst Performance

The synthesized catalysts were employed for the photo degradation of methylene blue dye under solar light irradiation. Firstly, degradation experiments were followed with the one-hour adsorption–desorption equilibrium tests in dark as well as in light. Figure 8a demonstrates the photo degradation efficiency of the catalysts for the degradation of methylene blue in 90 min experiment under natural solar light. To study the kinetics of the degradation process, $\ln(C_t/C_0)$ vs. irradiation time curve was plotted (Figure 8b). The graph shows the almost linear plots for all samples. The rate constant was determined from the slope of the $\ln(C_0/C_t)$ vs. time plots. The calculated rate constant follows the order as: Nd2 (0.0262) > Nd1 (0.013) > Nd0 (0.006) > Blank (0.001). Results indicate that Nd2 has the highest rate constant, followed by Nd1, which implies that Nd doping ions into the Ni–Zn matrix has resulted in an increase of the photo catalytic efficiencies of the catalyst. The observed value of photo degradation efficiency (98%) of Nd2 is quite promising for MB removal. We have compared the observed results with the previously reported results for MB removal using ferrite-based photo catalysts (Table 3). For comparison, it is worth noting that Nd2 catalyst has the capacity to degrade MB (20 mg L⁻¹) in merely 90 min while similar types of ferrite-based catalysts with the same catalyst dosage were able to degrade the similar dye concentration in more than 90 min. The regression coefficients and complete kinetic equations are shown in Table 4. From the table, it is clear that degradation using every catalyst follows the first order kinetics as regression coefficient values are approximately close to one.

Table 3. Comparison of previously reported work on MB degradation using ferrites and their composites.

Sr. No.	Photocatalyst	Light Source	Dye Concentration	Catalyst Dosage	Removal Efficiency (%) (Reaction Time)	Reference
1	MnFe ₂ O ₄ -GSC	Sunlight	10 mg L ⁻¹	0.25 g L ⁻¹	100 % (180 min)	[59]
2	ZnFe ₂ O ₄	UV-Visible, sunlight	10 mg L ⁻¹	0.1 g L ⁻¹	96% 85% (180 min)	[60]
3	NiCe _y Fe _{2-y} O ₄ /rGO	Visible light	5 mg L ⁻¹	0.5 g L ⁻¹	94.67 % (70 min)	[61]
4	CoFe ₂ O ₄ -CNT	visible light lamp	10 mg L ⁻¹	0.50 g L ⁻¹	97% (180 min)	[62]
5	CoFe ₂ O ₄ -rGO	visible light	10 mg L ⁻¹	0.50 g L ⁻¹	58% (180 min)	
6	NiCe _{0.05} Fe _{1.95} O ₄ @rGO	Xenon (200 W)	5 mg L ⁻¹	-	94.67% (70 min)	[61]
7	Ni _{0.96} Cd _{0.04} Gd _{0.04} Fe _{1.96} O ₄ /rGO	visible light	10 mg L ⁻¹	0.10 g L ⁻¹	92.27% (160 min)	[63]
8	NiFe ₂ O ₄	Halogen lamp (200 W)	10 mg L ⁻¹	-	98.23% (60 min)	[64]
9	Co _{0.1} Mg _{0.9} Fe ₂ O ₄ , MgFe ₂ O ₄	halogen lamp, sunlight	10 mg L ⁻¹	0.10 g g L ⁻¹	74.50%, 82% (240 min)	[65]
10	Ni _{0.5} Zn _{0.5} Nd _{0.05} Fe _{1.95} O ₄ (Nd2)	Solar-light	20 mg L ⁻¹	0.25 g L ⁻¹	98% (90 min)	This work

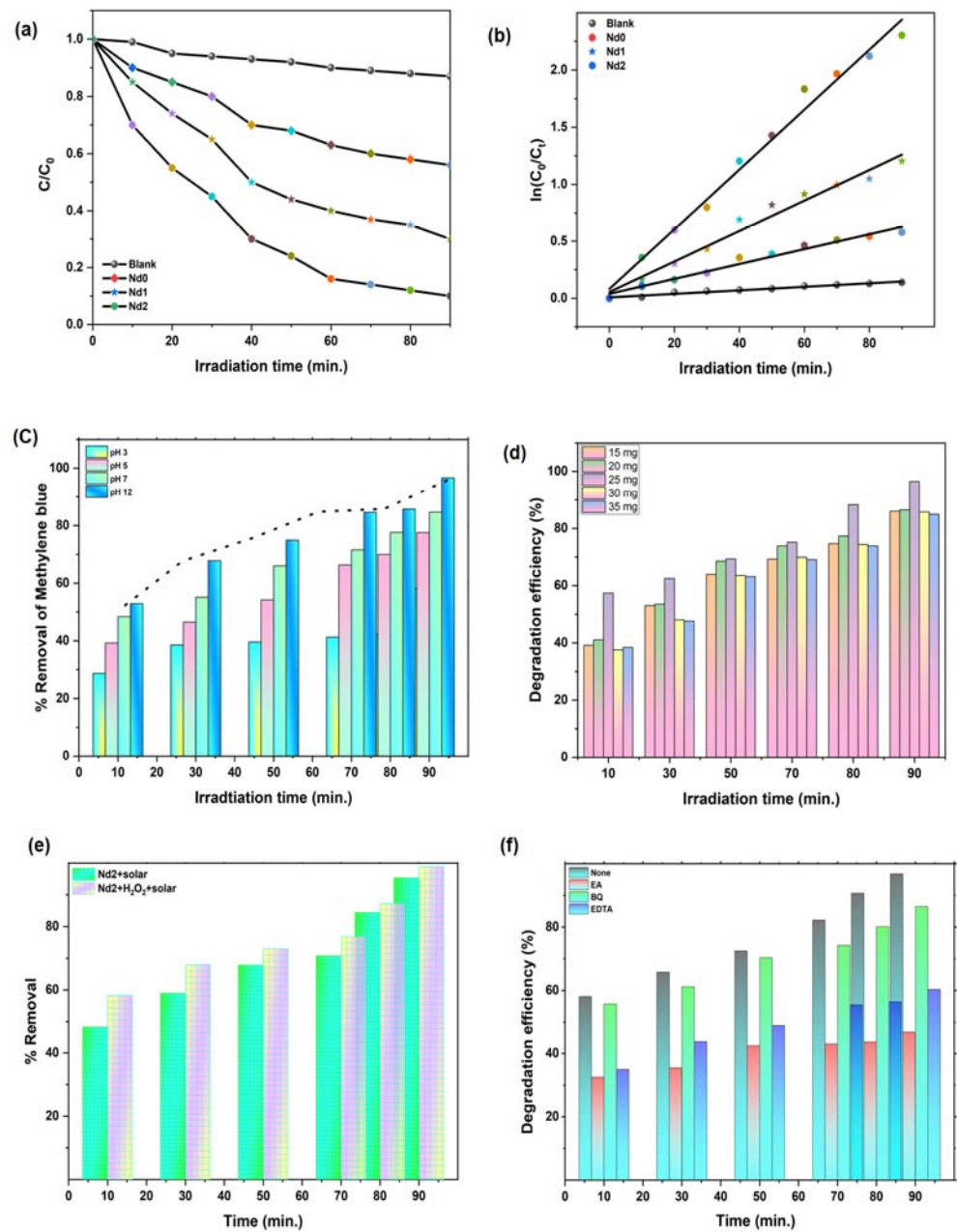


Figure 8. (a) C_t/C_0 vs. time curve for photo degradation of methylene blue. (b) Pseudo first order kinetics of photo degradation process. (c) Effect of pH of the medium on the degradation of methylene blue. (d) Effect of catalyst dose on the photo degradation of methylene blue (reaction parameter, pH-12, methylene blue concentration-0.20 mg/L). (e) Photo degradation of methylene blue with/without presence of H_2O_2 (pH-7: H_2O_2 volume-5 mL: methylene blue concentration-0.20 mg/L, catalyst dose: 25 mg). (f) Scavenging experiment for the determination of reactive species.

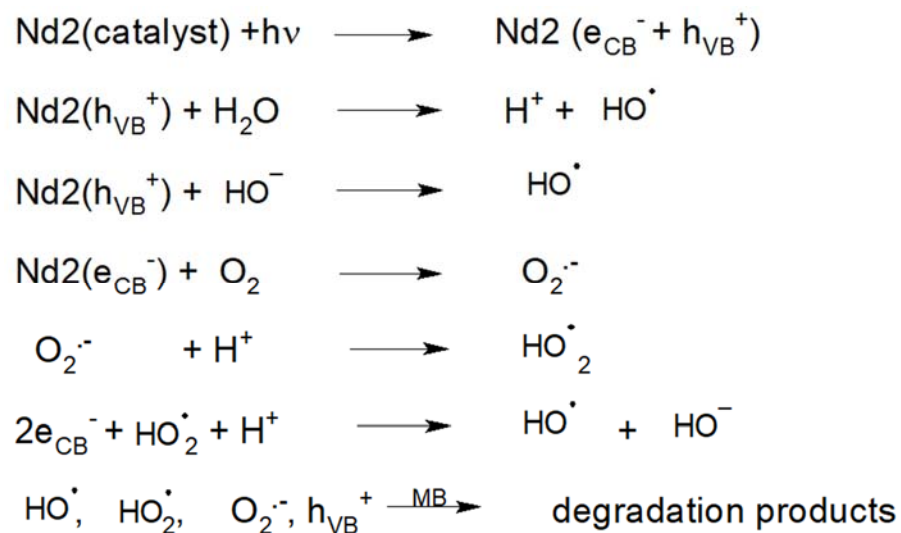
Table 4. Kinetics parameters derived from kinetics curves for degradation process.

Catalyst	Regression Coefficient (R^2)	Rate Constant (min.^{-1})	Kinetics Equation
Nd0	0.9720	0.0065	$0.0065 * x + 0.0390$
Nd1	0.9755	0.0133	$0.0133 * x + 0.0546$
Nd2	0.9869	0.0262	$0.0263 * x + 0.0814$

4.2. Effect of Reaction Parameters

The degradation process is extremely sensitive to the initial pH of the degradation medium. To examine the effect of pH on the degrading efficiency of the Nd2 catalyst, which emerges as the best catalyst from the kinetics research, a series of experiments were conducted with varying pH of the medium. The results of the pH variations on the photo catalytic degradation efficiency are shown in Figure 8c. The pH is varied over the range of 3–12 (acidic to basic) pH value. The degradation efficiency increases as the pH of medium transforms from 3 to 12. For the highly acidic medium, the degradation of methylene blue merely reaches up to 55% in 90 min experiment of degradation. However, it reaches up to 73%, 78%, and 96% for pH 5, 7, and 12, respectively. Such observed results reveal that highly basic medium is suitable for degradation of methylene blue using Nd doped Ni-Zn ferrite catalyst. The lower degradation efficiency at pH 7 is attributed to the charge neutralization at the surface of the catalyst. The highly acidic conditions seem not to be favorable as electrostatic forces restrict the interaction of catalyst surface and dye molecules [66]. However, in the observed results, basic conditions have shown a remarkable increase in the degradation efficiency.

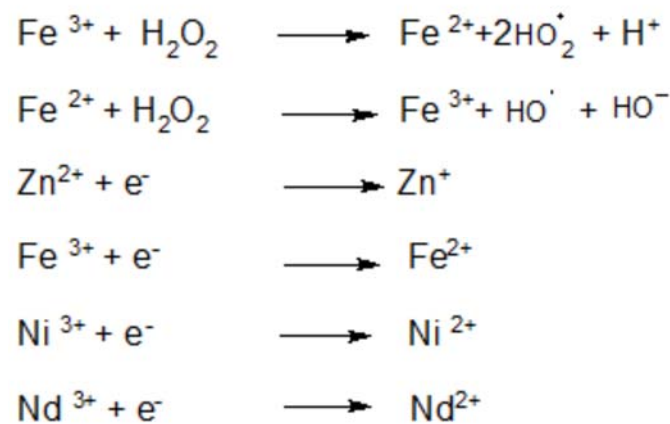
Among the reaction parameters affecting the degradation process, catalyst dose is a prime one. To further check the variation in photo degradation efficiency, we performed the degradation experiment with catalyst dosage ranging between 15–35 mg at pH-12 with fixed dye concentration of 20 mg/L. The observed degradation efficiency is shown in Figure 8d. The results reveal that the photo degradation efficiency was found to increase with the increase in catalyst dosage from 15–25 mg/L. The slightly decreased value of efficiency with a decreased amount of catalyst loading was assigned to the higher transmission of light through the solution. The degradation efficiency attains maximum value at 25 mg/L and further increase in drug dosage leads to a decrease in degradation rate. Furthermore, the amount of catalyst loading may result in pronounced scattering effects of light leading to restriction of transmission of light through the solution medium. The proposed catalyst exhibits a magnetic nature and any higher dosage of catalyst can lead to agglomeration. The agglomeration may result in elimination of active sites, thereby decreasing the degradation efficiency. The typical reactions which could be generating the reactive species for the degradation process are summarized in Scheme 1.



Scheme 1. Redox reactions involved in degradation of methylene blue.

The photo catalytic removal of methylene blue under solar light is also tested in the presence of H₂O₂. The obtained results are shown in Figure 8e. The observed results indicate that under solar light, Nd2 + H₂O₂ catalyst system is highly efficient for the degradation of MB as 98% degradation is observed under these reaction conditions. This

behavior directs us to believe in more hydroxyl radical generation through the photo-Fenton reactions. However, this contribution is small as the proposed catalyst is quite efficient without the presence of H_2O_2 . Scheme 2 shows some of the feasible reactions which take place in the presence of H_2O_2 .



Scheme 2. Feasible reactions for photo degradation of MB involving H_2O_2 using Nd2 catalyst.

4.3. Degradation Mechanism Insight

The photo catalytic degradation of organic pollutants is followed by reactive species such as superoxide radicals, hydroxyl radicals, or photo induced holes generated through conduction or valence bands [67]. To explore the mechanism of the degradation process, it is necessary to find out the reactive species involved in the process. For the said purpose, we performed the degradation experiment for methylene blue in presence of scavengers, namely iso-propyl alcohol (IPA), benzoquinone (BQ), and Ethylenediamine tetra acetic acid (EDTA) for presence of hydroxyl radical, superoxide radicals, and holes, respectively. Figure 8f shows that addition of BQ results in a slight decrease of degradation efficiency followed by EDTA. However, with the addition of IPA, degradation efficiency significantly changes from 98% (without scavenger) to 42%, indicating that $\bullet\text{OH}$ radical has the sound impact on the degradation efficiency. The results indicate that $\bullet\text{OH}$ radical is the primary reactive species followed by h^+ generated by EDTA. Such behavior is also supported by degradation experiment performed in the presence of H_2O_2 . We have discussed two possible schemes for degradation mechanism. The scavenging experiments have also confirmed $\bullet\text{OH}$ radical as the main reactive species. In the ferrites, photo-Fenton type reaction mechanisms are very common [68]. The increased photocatalytic activity for catalyst with Nd ions substitution at Fe sites may be assigned to various reasons. One reason may be moderate band gap value due to the inclusion of a new energy level just below the conduction band, when compared to other catalysts, which ensures optimal light absorption with lower recombination. A second reason is the Nd substitution effect at different sites, at Zn sites, and Fe sites. The Nd substitution at Fe sites have resulted in more charge transfer capacity which is a required condition for excellent photocatalytic activity of the catalysts. The lower carrier recombination rate for Nd2 is also supported through EIS results. Another possible reason could be the defects created by octahedrally coordinated Nd ions, which are responsible for enhanced catalytic activity. The octahedral sites occupied by large Nd^{3+} ions are more surface exposed and more catalytically active [69]. Moreover, Nd ions exhibit mixed valence state in Nd2 catalyst, which favors the charge transfer capacity of the catalyst. Thus, metal redox cycles, such as $\text{Nd}^{3+}/\text{Nd}^{2+}$ and $\text{Fe}^{2+}/\text{Fe}^{3+}$, could exist, which may act as mediators/facilitators for electron transfer to $\text{O}_2/\text{H}_2\text{O}$ to generated facile. The possible mechanism for degradation of methylene blue is shown in Figure 9a. Many important properties of an excellent photo catalyst rely on its reusability and recoverability, so it is quite necessary to perform degradation experiments over a number of cycles.

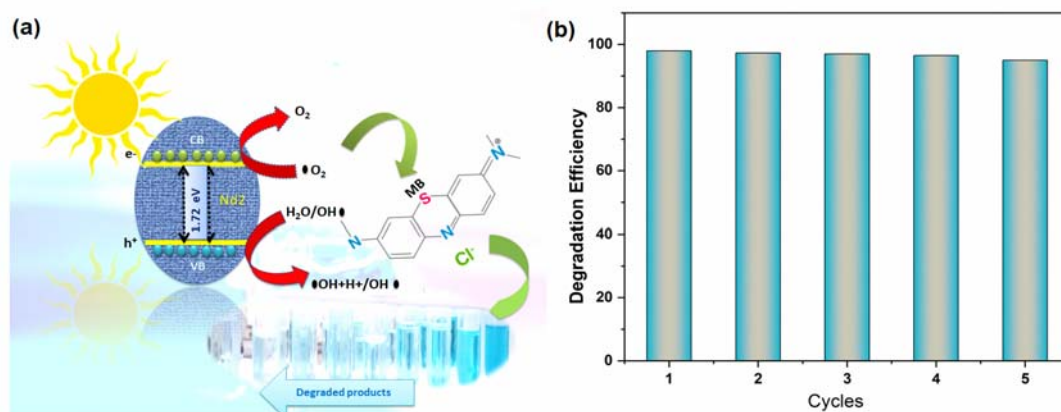


Figure 9. (a) Proposed mechanism for solar driven degradation of methylene blue using Nd₂ catalyst, (b) Reusability of Nd₂ catalyst over five successive cycles.

4.4. Stability and Reusability Studies

To further assure ourselves about the stability and reusability of the synthesized catalysts, Nd₂ catalysts were employed for the photo degradation experiment over five cycles. Figure 9b demonstrates the results of photo degradation experiments over five cycles run. The catalysts, being highly magnetic in nature, are easily recovered with the help of external magnetic field after each cycle and then, after drying, can be reutilized. The photo degradation efficiency decreases merely from 98 to 97.6% from the first to the second cycle. However, after five cycles of run, the degradation efficiency reaches 96.2%. There is no significant loss of catalyst performance even after five cycles. Such results indicate the prepared catalyst shows sound stability and can be utilized for the degradation of other organic pollutants as well.

5. Conclusions

To summarize, solar light-driven Nd-doped Ni-Zn ferrite nanoparticles were synthesized using the solution combustion method and used for methylene blue degradation. The synthesized ferrites were systematically characterized for structural, optical, and magnetic properties. Structural studies confirmed the pure phased structure for all compositions. Optical studies revealed the decrease in the band gap with Nd ions doping. Magnetic studies confirmed the highly magnetic nature of the catalysts. Ni_{0.5}Zn_{0.5}Nd_{0.5}Fe_{1.95}O₄ catalyst was found to exhibit maximum degradation efficiency (~98%) for methylene blue degradation. XPS analysis confirms the presence of oxygen vacancies and mixed valence states of metal ions in photo catalysts. The hydroxyl radical has been identified as a highly reactive species involved in the degradation process. Reactions and schemes involved in the degradation mechanism have been proposed based on these interpretations from various experiments. Moreover, the highly magnetic nature, stability, and reusability of the fabricated catalysts suggest their potential for utilization in the photo degradation of methylene blue and other organic pollutants as well.

Author Contributions: Conceptualization, P.D.; supervision, P.D.; contribution to original draft. G.R. and J.S.; data curation, investigation, E.A.D. review and editing, A.K. (Amit Kumar); writing—original draft. G.S.; writing—original draft, review and editing, A.K. (Arun Kumar); review and editing. All authors have read and agreed to the published version of the manuscript.

Funding: This research received no external funding.

Data Availability Statement: Data sharing not applicable.

Acknowledgments: This work was supported by the Shoolini University, India.

Conflicts of Interest: The authors declare no conflict of interest.

References

1. Kumar, A.; Kumar, A.; Sharma, G.; Al-Muhtaseb, A.a.H.; Naushad, M.; Ghfar, A.A.; Guo, C.; Stadler, F.J. Biochar-templated g-C₃N₄/Bi₂O₂CO₃/CoFe₂O₄ nano-assembly for visible and solar assisted photo-degradation of paraquat, nitrophenol reduction and CO₂ conversion. *Chem. Eng. J.* **2018**, *339*, 393–410. [[CrossRef](#)]
2. Jain, R.; Sikarwar, S. Photocatalytic and adsorption studies on the removal of dye Congo red from wastewater. *Int. J. Environ. Pollut.* **2006**, *27*, 158. [[CrossRef](#)]
3. Alshorifi, F.T.; Alswat, A.A.; Salama, R.S. Gold-selenide quantum dots supported onto cesium ferrite nanocomposites for the efficient degradation of rhodamine B. *Heliyon* **2022**, *8*, e09652. [[CrossRef](#)]
4. Muthuraman, G.; Teng, T.T. Extraction and recovery of rhodamine B, methyl violet and methylene blue from industrial wastewater using D2EHPA as an extractant. *J. Ind. Eng. Chem.* **2009**, *15*, 841–846. [[CrossRef](#)]
5. Kant, S.; Pathania, D.; Singh, P.; Dhiman, P.; Kumar, A. Removal of malachite green and methylene blue by Fe_{0.01}Ni_{0.01}Zn_{0.98}O/polyacrylamide nanocomposite using coupled adsorption and photocatalysis. *Appl. Catal. B Environ.* **2014**, *147*, 340–352. [[CrossRef](#)]
6. Li, S.; Lin, Q.; Liu, X.; Yang, L.; Ding, J.; Dong, F.; Li, Y.; Irfan, M.; Zhang, P. Fast photocatalytic degradation of dyes using low-power laser-fabricated Cu₂O-Cu nanocomposites. *RSC Adv.* **2018**, *8*, 20277–20286. [[CrossRef](#)]
7. Khan, I.; Saeed, K.; Zekker, I.; Zhang, B.; Hendi, A.H.; Ahmad, A.; Ahmad, S.; Zada, N.; Ahmad, H.; Shah, L.A.; et al. Review on Methylene Blue: Its Properties, Uses, Toxicity and Photodegradation. *Water* **2022**, *14*, 242. [[CrossRef](#)]
8. Sharma, S.; Sharma, G.; Kumar, A.; Dhiman, P.; AlGarni, T.S.; Naushad, M.; Allothman, Z.A.; Stadler, F.J. Controlled synthesis of porous Zn/Fe based layered double hydroxides: Synthesis mechanism, and ciprofloxacin adsorption. *Sep. Purif. Technol.* **2021**, *278*, 119481. [[CrossRef](#)]
9. Natarajan, S.; Bajaj, H.C.; Tayade, R.J. Recent advances based on the synergetic effect of adsorption for removal of dyes from waste water using photocatalytic process. *J. Environ. Sci.* **2018**, *65*, 201–222. [[CrossRef](#)]
10. Gupta, V.K.; Kumar, R.; Nayak, A.; Saleh, T.A.; Barakat, M.A. Adsorptive removal of dyes from aqueous solution onto carbon nanotubes: A review. *Adv. Colloid Interface Sci.* **2013**, *193*, 24–34. [[CrossRef](#)]
11. Dhiman, P.; Patial, M.; Kumar, A.; Alam, M.; Naushad, M.; Sharma, G.; Vo, D.-V.N.; Kumar, R. Environmental friendly and robust Mg_{0.5-x}Cu_xZn_{0.5}Fe₂O₄ spinel nanoparticles for visible light driven degradation of Carbamazepine: Band shift driven by dopants. *Mater. Lett.* **2020**, *284*, 129005. [[CrossRef](#)]
12. Dhiman, P.; Kumar, A.; Shekh, M.; Sharma, G.; Rana, G.; Vo, D.-V.N.; AlMasoud, N.; Naushad, M.; Allothman, Z.A. Robust magnetic ZnO-Fe₂O₃ Z-scheme heterojunctions with in-built metal-redox for high performance photo-degradation of sulfamethoxazole and electrochemical dopamine detection. *Environ. Res.* **2021**, *197*, 111074. [[CrossRef](#)]
13. Gupta, V.K.; Jain, R.; Mittal, A.; Saleh, T.A.; Nayak, A.; Agarwal, S.; Sikarwar, S. Photo-catalytic degradation of toxic dye amaranth on TiO₂/UV in aqueous suspensions. *Mater. Sci. Eng. C* **2012**, *32*, 12–17. [[CrossRef](#)]
14. Cevallos-Mendoza, J.; Amorim, C.G.; Rodríguez-Díaz, J.M.; Montenegro, M.D.C.B.S.M. Removal of Contaminants from Water by Membrane Filtration: A Review. *Membranes* **2022**, *12*, 570. [[CrossRef](#)]
15. Kour, S.; Jasrotia, R.; Puri, P.; Verma, A.; Sharma, B.; Singh, V.P.; Kumar, R.; Kalia, S. Improving photocatalytic efficiency of MnFe₂O₄ ferrites via doping with Zn²⁺/La³⁺ ions: Photocatalytic dye degradation for water remediation. *Environ. Sci. Pollut. Res.* **2021**, 1–16. [[CrossRef](#)]
16. Saravanan, A.; Kumar, P.S.; Vo, D.-V.N.; Yaashikaa, P.R.; Karishma, S.; Jeevanantham, S.; Gayathri, B.; Bharathi, V.D. Photocatalysis for removal of environmental pollutants and fuel production: A review. *Environ. Chem. Lett.* **2021**, *19*, 441–463. [[CrossRef](#)]
17. Im, J.K.; Sohn, E.J.; Kim, S.; Jang, M.; Son, A.; Zoh, K.-D.; Yoon, Y. Review of MXene-based nanocomposites for photocatalysis. *Chemosphere* **2020**, *270*, 129478. [[CrossRef](#)]
18. Kumar, A.; Sharma, G.; Naushad, M.; Al-Muhtaseb, A.H.; García-Peñas, A.; Mola, G.T.; Si, C.; Stadler, F.J. Bio-inspired and biomaterials-based hybrid photocatalysts for environmental detoxification: A review. *Chem. Eng. J.* **2019**, *382*, 122937. [[CrossRef](#)]
19. Mudhoo, A.; Paliya, S.; Goswami, P.; Singh, M.; Lofrano, G.; Carotenuto, M.; Carraturo, F.; Libralato, G.; Guida, M.; Usman, M.; et al. Fabrication, functionalization and performance of doped photocatalysts for dye degradation and mineralization: A review. *Environ. Chem. Lett.* **2020**, *18*, 1825–1903. [[CrossRef](#)]
20. Naushad, M.; Vasudevan, S.; Sharma, G.; Kumar, A.; Allothman, Z.A. Adsorption kinetics, isotherms, and thermodynamic studies for Hg²⁺ adsorption from aqueous medium using alizarin red-S-loaded amberlite IRA-400 resin. *Desalination Water Treat.* **2016**, *57*, 18551–18559. [[CrossRef](#)]
21. Dhiman, P.; Kumar, G.; Batoor, K.; Kumar, A.; Sharma, G.; Singh, M. Effective Degradation of Methylene Blue using ZnO: Fe: Ni Nanocomposites. *Mater. Res. Found.* **2018**, *29*.
22. Dhiman, P.; Dhiman, N.; Kumar, A.; Sharma, G.; Naushad, M.; Ghfar, A.A. Solar active nano-Zn_{1-x}Mg_xFe₂O₄ as a magnetically separable sustainable photocatalyst for degradation of sulfadiazine antibiotic. *J. Mol. Liq.* **2019**, *294*, 111574. [[CrossRef](#)]
23. Akhtar, M.N.; Nazir, M.S.; Khan, M.A.; Ullah, S.; Assiri, M.A. Preparations and characterizations of Ca doped Ni-Mg-Mn nanocrystalline ferrites for switching field high-frequency applications. *Ceram. Int.* **2021**, *48*, 3833–3840. [[CrossRef](#)]
24. Dhiman, P.; Rana, G.; Alshgari, R.A.; Kumar, A.; Sharma, G.; Naushad, M.; Allothman, Z.A. Magnetic Ni-Zn ferrite anchored on g-C₃N₄ as nano-photocatalyst for efficient photo-degradation of doxycycline from water. *Environ. Res.* **2023**, *216*, 114665. [[CrossRef](#)] [[PubMed](#)]

25. Alshorifi, F.T.; Ali, S.L.; Salama, R.S. Promotional Synergistic Effect of Cs–Au NPs on the Performance of Cs–Au/MgFe₂O₄ Catalysts in Catalysis 3,4-Dihydropyrimidin-2(1H)-Ones and Degradation of RhB Dye. *J. Inorg. Organomet. Polym. Mater.* **2022**, *32*, 3765–3776. [[CrossRef](#)]
26. Mugutkar, A.B.; Gore, S.K.; Patange, S.M.; Mane, R.S.; Raut, S.D.; Shaikh, S.F.; Ubaidullah, M.; Pandit, B.; Jadhav, S.S. Ammonia gas sensing and magnetic permeability of enhanced surface area and high porosity lanthanum substituted Co–Zn nano ferrites. *Ceram. Int.* **2022**, *48*, 15043–15055. [[CrossRef](#)]
27. Jamir, M.; Alam, A.; Borah, J.P. Advancement of Spinel Ferrites for Biomedical Application. In *Nanoscale Engineering of Biomaterials: Properties and Applications*; Pandey, L.M., Hasan, A., Eds.; Springer Nature Singapore: Singapore, 2022; pp. 227–253.
28. Tobbala, D.E.; Rashed, A.S.; Salama, R.S.; Ahmed, T.I. Performance enhancement of reinforced concrete exposed to electrochemical magnesium chloride using nano-ferrite zinc-rich epoxy. *J. Build. Eng.* **2022**, *57*, 104869. [[CrossRef](#)]
29. Dhiman, P. Hexagonal Ferrites, Synthesis, Properties and Their Applications. *Mater. Res. Found.* **2021**, *112*, 336.
30. Miri, A.; Sarani, M.; Najafidoust, A.; Varma, R.S. Evaluation of photocatalytic performance and cytotoxic activity of green synthesized nickel ferrite nanoparticles. *Environ. Prog. Sustain. Energy* **2021**, *41*, e13757. [[CrossRef](#)]
31. Hong, D.; Yamada, Y.; Nagatomi, T.; Takai, Y.; Fukuzumi, S. Catalysis of nickel ferrite for photocatalytic water oxidation using [Ru (bpy)₃]²⁺ and S₂O₈²⁻. *J. Am. Chem. Soc.* **2012**, *134*, 19572–19575. [[CrossRef](#)]
32. Kumari, P.S.; Charan, G.V.; Kumar, D.R. Synthesis, structural, photocatalytic and anti-cancer activity of Zn doped Ni nano chromites by citrate gel auto combustion method. *Inorg. Chem. Commun.* **2022**, *139*, 109393. [[CrossRef](#)]
33. Mosleh, M. Synthesis, characterization and optical properties of neodymium doped nickel ferrite nanoparticles prepared by novel sol–gel method. *J. Mater. Sci. Mater. Electron.* **2016**, *27*, 6703–6707. [[CrossRef](#)]
34. Chaudhari, N.D.; Nadargi, D.Y.; Kabbur, S.M.; Kambale, R.C.; Das, A.; Suryavanshi, S.S. Investigation of Structural, Morphological and Elastic Properties of Ni–Zn Ferrite Grown with an Oxalate Precursor. *J. Electron. Mater.* **2022**, *51*, 2732–2740. [[CrossRef](#)]
35. Chehade, W.; Basma, H.; Abdallah, A.; Hassan, R.S.; Awad, R. Synthesis and magneto-optical studies of novel Ni_{0.5}Zn_{0.5}Fe₂O₄/Zn_{0.95}Co_{0.05}O nanocomposite as a candidate for photocatalytic applications. *Ceram. Int.* **2021**, *48*, 1238–1255. [[CrossRef](#)]
36. Kumar, N.H.; Ravinder, D.; Babu, T.A.; Venkatesh, N.; Swathi, S.; Prasad, N.K. Development of Cu²⁺ substituted Ni–Zn ferrite nano-particles and their high-temperature semiconductor behaviour. *J. Indian Chem. Soc.* **2022**, *99*, 100362. [[CrossRef](#)]
37. Upadhyay, C.; Mishra, D.; Verma, H.; Anand, S.; Das, R. Effect of preparation conditions on formation of nanophase Ni–Zn ferrites through hydrothermal technique. *J. Magn. Magn. Mater.* **2003**, *260*, 188–194. [[CrossRef](#)]
38. Dhiman, P.; Rana, G.; Kumar, A.; Sharma, G.; Vo, D.-V.N.; AlGarni, T.S.; Naushad, M.; Alothman, Z.A. Nanostructured magnetic inverse spinel Ni–Zn ferrite as environmental friendly visible light driven photo-degradation of levofloxacin. *Chem. Eng. Res. Des.* **2021**, *175*, 85–101. [[CrossRef](#)]
39. Vergis, B.R.; Kottam, N.; Krishna, R.H.; Kumar, G.A. Comparison of magnetic and dielectric properties of transition metal nanospinel ferrites, MFe₂O₄, (M = Co, Cu, Ni, Zn) synthesized by one-pot combustion route. *Mater. Today Proc.* **2021**, *49*, 870–877. [[CrossRef](#)]
40. Dhiman, P.; Sharma, G.; Alodhayb, A.N.; Kumar, A.; Rana, G.; Sithole, T.; Alothman, Z.A. Constructing a Visible-Active CoFe₂O₄@Bi₂O₃/NiO Nanoheterojunction as Magnetically Recoverable Photocatalyst with Boosted Ofloxacin Degradation Efficiency. *Molecules* **2022**, *27*, 8234. [[CrossRef](#)]
41. Zhang, S.; Wu, J.; Li, F.; Li, L. Enhanced photocatalytic performance of spinel ferrite (MFe₂O₄, M = Zn, Mn, Co, Fe, Ni) catalysts: The correlation between morphology–microstructure and photogenerated charge efficiency. *J. Environ. Chem. Eng.* **2022**, *10*, 107702. [[CrossRef](#)]
42. Hammouche, J.; Gaidi, M.; Columbus, S.; Omari, M. Enhanced Photocatalytic Performance of Zinc Ferrite Nanocomposites for Degrading Methylene Blue: Effect of Nickel Doping Concentration. *J. Inorg. Organomet. Polym. Mater.* **2021**, *31*, 3496–3504. [[CrossRef](#)]
43. Harish, K.N.; Bhojya Naik, H.S.; Prashanth kumar, P.N.; Viswanath, R. Optical and Photocatalytic Properties of Solar Light Active Nd-Substituted Ni Ferrite Catalysts: For Environmental Protection. *ACS Sustain. Chem. Eng.* **2013**, *1*, 1143–1153. [[CrossRef](#)]
44. Adam, M.S.S.; Hafez, A.M.; Khalaf, M.M. Rare earth Ce- and Nd-doped spinel nickel ferrites as effective heterogeneous catalysts in the (ep)oxidation of alkenes. *J. Iran. Chem. Soc.* **2020**, *17*, 3237–3250. [[CrossRef](#)]
45. Vosoughifar, M.; Kimiay, A. Neodymium-doped copper ferrite: Auto-combustion synthesis, characterization and photocatalytic properties. *J. Mater. Sci. Mater. Electron.* **2016**, *27*, 10031–10035. [[CrossRef](#)]
46. Kaur, A.; Salunke, D.B.; Umar, A.; Mehta, S.K.; Sinha, A.S.K.; Kansal, S.K. Visible light driven photocatalytic degradation of fluoroquinolone levofloxacin drug using Ag₂O/TiO₂ quantum dots: A mechanistic study and degradation pathway. *New J. Chem.* **2017**, *41*, 12079–12090. [[CrossRef](#)]
47. Dhiman, P.; Mehta, T.; Kumar, A.; Sharma, G.; Naushad, M.; Ahamad, T.; Mola, G.T. Mg_{0.5}Ni_xZn_{0.5-x}Fe₂O₄ spinel as a sustainable magnetic nano-photocatalyst with dopant driven band shifting and reduced recombination for visible and solar degradation of Reactive Blue-19. *Adv. Powder Technol.* **2020**, *31*, 4585–4597. [[CrossRef](#)]
48. Kumar, S.; Singh, V.; Aggarwal, S.; Mandal, U.K.; Kotnala, R. Synthesis of nanocrystalline Ni_{0.5}Zn_{0.5}Fe₂O₄ ferrite and study of its magnetic behavior at different temperatures. *Mater. Sci. Eng. B* **2010**, *166*, 76–82. [[CrossRef](#)]
49. Ateia, E.E.; Ahmed, M.; Salah, L.; El-Gamal, A. Effect of rare earth oxides and La³⁺ ion concentration on some properties of Ni–Zn ferrites. *Phys. B Condens. Matter* **2014**, *445*, 60–67. [[CrossRef](#)]

50. Jadhav, S.A.; Somvanshi, S.B.; Khedkar, M.V.; Patade, S.R.; Jadhav, K.M. Magneto-structural and photocatalytic behavior of mixed Ni–Zn nano-spinel ferrites: Visible light-enabled active photodegradation of rhodamine B. *J. Mater. Sci. Mater. Electron.* **2020**, *31*, 11352–11365. [[CrossRef](#)]
51. Mariosi, F.R.; Venturini, J.; Viegas, A.D.C.; Bergmann, C.P. Lanthanum-doped spinel cobalt ferrite (CoFe₂O₄) nanoparticles for environmental applications. *Ceram. Int.* **2020**, *46*, 2772–2779. [[CrossRef](#)]
52. Gupta, N.K.; Ghaffari, Y.; Kim, S.; Bae, J.; Kim, K.S.; Saifuddin, M. Photocatalytic Degradation of Organic Pollutants over MFe₂O₄ (M = Co, Ni, Cu, Zn) Nanoparticles at Neutral pH. *Sci. Rep.* **2020**, *10*, 4942. [[CrossRef](#)]
53. Dhiman, P.; Chand, J.; Verma, S.; Sarveena; Singh, M.P. Ni, Fe Co-doped ZnO nanoparticles synthesized by solution combustion method. *AIP Conf. Proc.* **2014**, *1591*, 1443–1445.
54. Torchynska, T.; Vega Macotela, L.; Khomenkova, L.; Goubilleau, F.; Lartundo Rojas, L. Annealing impact on emission and phase varying of Nd-doped Si-rich-HfO₂ films prepared by RF magnetron sputtering. *J. Mater. Sci. Mater. Electron.* **2020**, *31*, 4587–4594. [[CrossRef](#)]
55. Zhang, Y.; Chen, Y.; Kou, Q.; Wang, Z.; Han, D.; Sun, Y.; Yang, J.; Liu, Y.; Yang, L. Effects of Nd concentration on structural and magnetic properties of ZnFe₂O₄ nanoparticles. *J. Mater. Sci. Mater. Electron.* **2017**, *29*, 3665–3671. [[CrossRef](#)]
56. Qian, K.; Yao, Z.; Lin, H.; Zhou, J.; Haidry, A.A.; Qi, T.; Chen, W.; Guo, X. The influence of Nd substitution in Ni–Zn ferrites for the improved microwave absorption properties. *Ceram. Int.* **2019**, *46*, 227–235. [[CrossRef](#)]
57. Somnath; Sharma, I.; Kotnala, R.K.; Singh, M.; Kumar, A.; Dhiman, P.; Singh, V.P.; Verma, K.; Kumar, G. Structural, magnetic and Mössbauer studies of Nd-doped Mg-Mn ferrite nanoparticles. *J. Magn. Magn. Mater.* **2017**, *444*, 77–86. [[CrossRef](#)]
58. Dalal, M.; Mallick, A.; Mahapatra, A.; Mitra, A.; Das, A.; Das, D.; Chakrabarti, P. Effect of cation distribution on the magnetic and hyperfine behaviour of nanocrystalline Co doped Ni–Zn ferrite (Ni_{0.4}Zn_{0.4}Co_{0.2}Fe₂O₄). *Mater. Res. Bull.* **2016**, *76*, 389–401. [[CrossRef](#)]
59. Luciano, A.J.R.; Soletti, L.D.S.; Ferreira, M.E.C.; Cusioli, L.F.; de Andrade, M.B.; Bergamasco, R.; Yamaguchi, N.U. Manganese ferrite dispersed over graphene sand composite for methylene blue photocatalytic degradation. *J. Environ. Chem. Eng.* **2020**, *8*, 104191. [[CrossRef](#)]
60. Ali, N.; Zada, A.; Zahid, M.; Ismail, A.; Rafiq, M.; Riaz, A.; Khan, A. Enhanced photodegradation of methylene blue with alkaline and transition-metal ferrite nanophotocatalysts under direct sun light irradiation. *J. Chin. Chem. Soc.* **2018**, *66*, 402–408. [[CrossRef](#)]
61. Rahman, A.; Warsi, M.F.; Shakir, I.; Shahid, M.; Zulfiqar, S. Fabrication of Ce³⁺ substituted nickel ferrite-reduced graphene oxide heterojunction with high photocatalytic activity under visible light irradiation. *J. Hazard. Mater.* **2020**, *394*, 122593. [[CrossRef](#)]
62. Jelokhani, F.; Sheibani, S.; Ataie, A. Adsorption and photocatalytic characteristics of cobalt ferrite-reduced graphene oxide and cobalt ferrite-carbon nanotube nanocomposites. *J. Photochem. Photobiol. A Chem.* **2020**, *403*, 112867. [[CrossRef](#)]
63. Rahman, A.; Zulfiqar, S.; Haq, A.U.; Alsafari, I.A.; Qazi, U.Y.; Warsi, M.F.; Shahid, M. Cd-Gd-doped nickel spinel ferrite nanoparticles and their nanocomposites with reduced graphene oxide for catalysis and antibacterial activity studies. *Ceram. Int.* **2020**, *47*, 9513–9521. [[CrossRef](#)]
64. Jadhav, S.A.; Khedkar, M.V.; Somvanshi, S.B.; Jadhav, K. Magnetically retrievable nanoscale nickel ferrites: An active photocatalyst for toxic dye removal applications. *Ceram. Int.* **2021**, *47*, 28623–28633. [[CrossRef](#)]
65. Dojcinovic, M.P.; Vasiljevic, Z.Z.; Pavlovic, V.P.; Barisic, D.; Pajic, D.; Tadic, N.B.; Nikolic, M.V. Mixed Mg–Co spinel ferrites: Structure, morphology, magnetic and photocatalytic properties. *J. Alloy. Compd.* **2021**, *855*, 157429. [[CrossRef](#)]
66. Sharma, G.; Kumar, A.; Naushad, M.; Dhiman, P.; Thakur, B.; García-Peñas, A.; Stadler, F.J. Gum Acacia-Crosslinked-Poly (Acrylamide) Hydrogel Supported C₃N₄/BiOI Heterostructure for Remediation of Noxious Crystal Violet Dye. *Materials* **2022**, *15*, 2549. [[CrossRef](#)]
67. Dhiman, P.; Naushad, M.; Batoor, K.M.; Kumar, A.; Sharma, G.; Ghfar, A.A.; Kumar, G.; Singh, M. Nano Fe_xZn_{1-x}O as a tuneable and efficient photocatalyst for solar powered degradation of bisphenol A from aqueous environment. *J. Clean. Prod.* **2017**, *165*, 1542–1556. [[CrossRef](#)]
68. Sharma, R.; Bansal, S.; Singhal, S. Tailoring the photo-Fenton activity of spinel ferrites (MFe₂O₄) by incorporating different cations (M = Cu, Zn, Ni and Co) in the structure. *Rsc Adv.* **2015**, *5*, 6006–6018. [[CrossRef](#)]
69. Abdo, M.; El-Daly, A. Sm-substituted copper-cobalt ferrite nanoparticles: Preparation and assessment of structural, magnetic and photocatalytic properties for wastewater treatment applications. *J. Alloy. Compd.* **2021**, *883*, 160796. [[CrossRef](#)]

Disclaimer/Publisher’s Note: The statements, opinions and data contained in all publications are solely those of the individual author(s) and contributor(s) and not of MDPI and/or the editor(s). MDPI and/or the editor(s) disclaim responsibility for any injury to people or property resulting from any ideas, methods, instructions or products referred to in the content.